Mechanisms of a Meteorological Drought Onset: Summer 2020 to Spring 2021 in Southwestern North America

RICHARD SEAGER,[a] MINGFANG TING,[a] PATRICK ALEXANDER,[a] JENNIFER NAKAMURA,[a] HAIBO LIU,[a] CUIHUA LI,[a] AND ISLA R. SIMPSON[b]

[a] *Lamont Doherty Earth Observatory of Columbia University, Palisades, New York*
[b] *National Center for Atmospheric Research, Boulder, Colorado*

(Manuscript received 28 April 2022, in final form 15 July 2022)

ABSTRACT: By summer 2021 moderate to exceptional drought impacted 28% of North America, focused west of the Mississippi, with serious impacts on fire, water resources, and agriculture. Here, using reanalyses and SST-forced climate models, we examine the onset and development of this southwestern drought from its inception in summer 2020 through winter and spring 2020/21. The drought severity in summer 2021 resulted from four consecutive prior seasons in which precipitation in the southwest United States was the lowest on record or, at least, extremely dry. The dry conditions in summer 2020 arose from internal atmospheric variability but are beyond the range of what the studied atmosphere models simulate for that season. From winter 2020 through spring 2021 the worsening drought conditions were guided by the development of a La Niña in the tropical Pacific Ocean. Decadal variability in the Pacific Ocean aided drought in the southern part of the region by driving the cool season to be drier during the last two decades. There is also evidence that the southern part of the region in spring is drying due to human-driven climate change. In sum the drought onset was driven by a combination of internal atmospheric variability and interannual climate variability and aided by natural decadal variability and human-driven climate change.

KEYWORDS: North America; Atmosphere-ocean interaction; Drought; Climate change; Climate variability; Decadal variability; Interannual variability

1. Introduction

At the end of summer 2021 the U.S. Drought Monitor reported that "90% of the West region (including Colorado and Wyoming) is characterized as 'in drought' with 54% in Extreme Drought or Exceptional Drought" (https://cpo.noaa.gov/News/ArtMID/7875/ArticleID/2642/What-Caused-The-Summer-2020-to-Spring-2021-Drought-in-Southwestern-North-America). Amidst multiple and widespread impacts, the Dixie fire in California became the second largest in the state's history and reservoir levels were low across almost the whole U.S. West including at the Colorado River's Lake Powell and Lake Mead at just 31% and 35% of capacity, respectively. Multiple states rated most of their rangelands and pasture in poor to very poor conditions and in October a statewide drought emergency was declared for California. Drought extended from northern Mexico into western Canada and from the Pacific Ocean to the Great Plains. Notably, the drought was intense in the Southwest despite large areas of above-normal precipitation in the summer of 2021 while the highest temperature anomalies were in the Pacific Northwest and western Canada (Fig. 1). This reflects that the severity of drought in summer 2021 was largely due to the preceding seasons. Drought rapidly onset in the summer of 2020 (Hoell et al. 2022) and intensified in the fall of 2020, winter 2020/21, and spring of 2021 [Fig. 1d; also see the report of the National Oceanic and Atmospheric Administration Drought Task Force in Mankin et al. (2021)]. This set the stage for the high-impact drought of summer 2021. Here we examine what large-scale atmosphere–ocean conditions were responsible for the onset and intensification of this latest widespread and severe drought in southwestern North America.

Drought over southwestern North America is invariably caused by persistent high pressure that induces northerly flow reducing moisture supply from the Pacific and Atlantic Oceans and subsidence that favors drying and enhanced static stability, and diverts away moisture-bearing synoptic systems. In a review Seager and Hoerling (2014), using observations and models and examining annual mean precipitation, claimed that internal atmosphere variability was responsible for most of such drought-inducing circulation variability. However, they also noted that sea surface temperature (SST) variability drove a substantial fraction of annual mean precipitation variability focused in the southern plains but also across most of southern North America. Previously, based on coordinated model simulations by many groups, the pioneering study of Schubert et al. (2009) showed that ideal conditions for drought in southwest North America were a cold tropical Pacific and warm tropical North Atlantic Ocean, a conclusion that has been validated since. Hence, the tropical oceans play a significant role in driving drought variability over southwestern North America and in the Great Plains. Given that tropical SSTs vary on seasonal to multidecadal time scales, this translates into precipitation variability on seasonal to multidecadal time scales as well, as has now been well established in examinations of drought history using

Supplemental information related to this paper is available at the Journals Online website: https://doi.org/10.1175/JCLI-D-22-0314.s1

Corresponding author: Richard Seager, seager@ldeo.columbia.edu

DOI: 10.1175/JCLI-D-22-0314.1

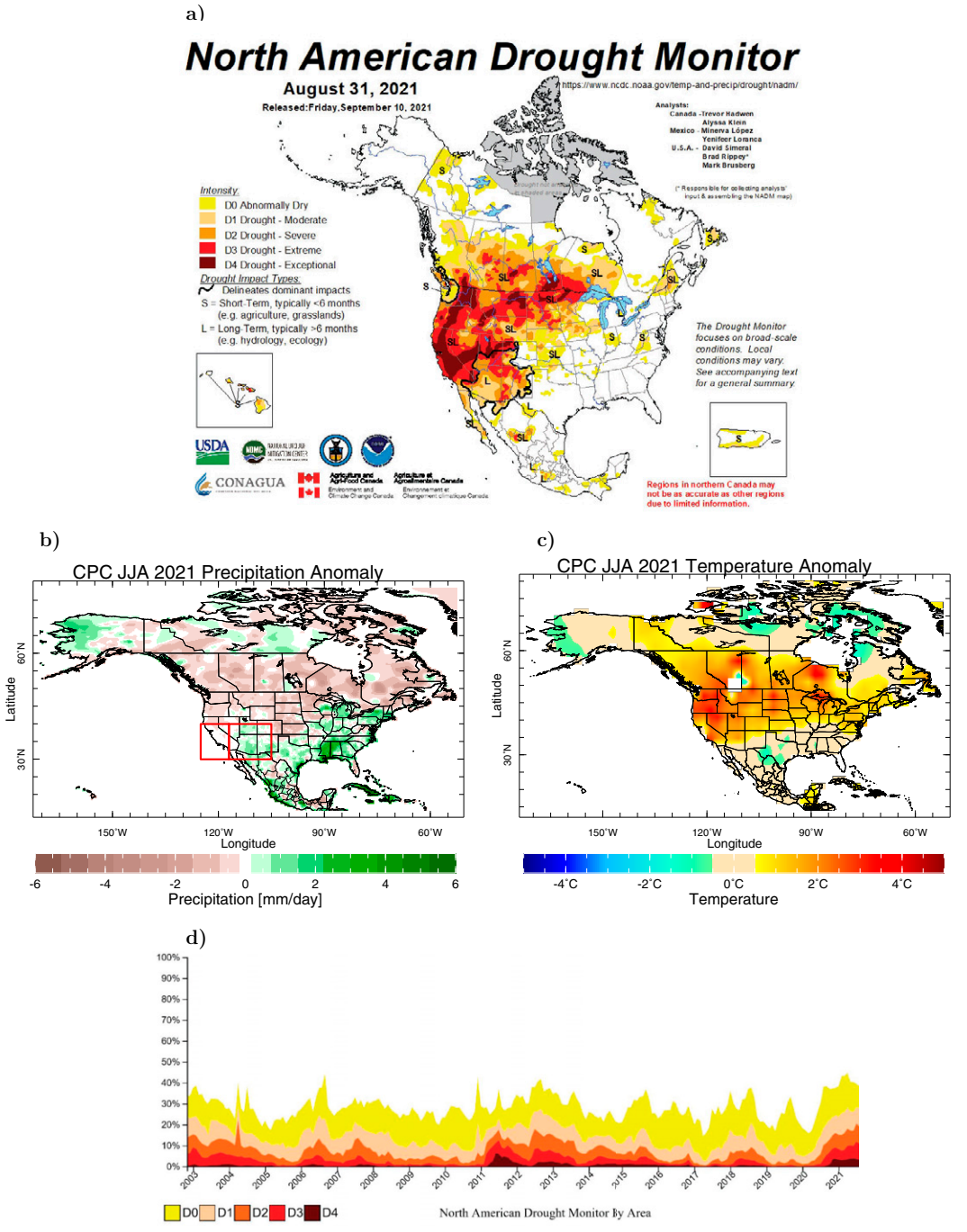

FIG. 1. (a) The North American Drought Monitor status report for 31 Aug 2021, together with CPC observed (b) precipitation and (c) temperature anomalies for JJA 2021 and (d) the percentage of North America in drought over November 2002–August 2021 as estimated by the Drought Monitor. The southwestern region studied and its division into coastal and interior subregions are shown in (b). (The white square in the temperature plots over Alberta results from missing data.)

observations and tree ring records over the last millennium (Schubert et al. 2004a,b; Seager et al. 2005; Herweijer et al. 2006; Huang et al. 2005; Cook et al. 2007; Seager et al. 2008; Hoerling et al. 2010; Feng et al. 2008; Shin et al. 2010; Shin and Sardeshmukh 2011; Delworth et al. 2015).

For the first two decades of the twenty-first century, southwestern North America has been in near-perpetual drought, which has rivaled the great megadroughts of the medieval period (Xiao et al. 2018; Hoerling et al. 2019; Williams et al. 2020, 2022). The causes of this drought, which has followed a very wet

1980s and 1990s (Swetnam and Betancourt 1998; Huang et al. 2005; Seager 2015), are much debated but many researchers agree that the associated precipitation decline has been influenced by the cool tropical Pacific phase of Pacific decadal variability (Seager and Hoerling 2014; Delworth et al. 2015; Lehner et al. 2018) while the associated warming is significantly human induced (Lehner et al. 2018) and has turned an ordinary decadal drought into a megadrought comparable to the medieval ones (Williams et al. 2020, 2022). Higher temperatures impact drought by increasing atmospheric water vapor holding capacity and, hence, evaporative demand. This can draw moisture from soils and vegetation, provided the extracted moisture is diverged away by the atmosphere [see, e.g., Ting et al. (2021) for how increased transient eddy moisture flux divergence enables soil drying over the Midwest in summer].

The apparent important role of natural Pacific decadal variability however does not exclude the possibility of human-induced precipitation changes also being important, either already or in the near future. Climate models predict reduced precipitation in the southern ranges of southwestern North America in midwinter and, more robustly, a reduction in precipitation across the Southwest and West Coast in spring (Seager et al. 2014b; Gao et al. 2014; Maloney et al. 2014; Ting et al. 2018). However, since the tropical Pacific plays an active role in the hydroclimate of southwest North America it should be noted that these projections are from models that systematically do not reproduce the observed lack of warming in the equatorial Pacific cold tongue (Seager et al. 2019a, 2022). It has been suggested that the observed trend toward an enhanced zonal SST gradient across the tropical Pacific is a response to radiative forcing that models misrepresent and also that it favors a high pressure ridge at the West Coast and drying (Seager et al. 2017).

Figure 1a shows that the recent drought across the West covers a vast area that includes several climate regimes. Along the west coast there is a Mediterranean-type climate with winter precipitation and warm-to-hot dry summers. But the drought extended into the interior West where there are both winter rains and a summer precipitation peak that might be thought of as a northward extension of the North American monsoon (Douglas et al. 1993; Adams and Comrie 1997). The easiest way to have a meteorological drought that covers both areas would be to have a common driver that reduces winter precipitation augmented by drought-inducing circulation anomalies that inhibit summer precipitation in the interior.

Against this background, here we consider the physical processes that caused the precipitation decline that led to drought onset and intensification from summer 2020 to spring 2021. Using observations and models we will attempt to ascertain the roles of internal atmospheric variability, SST forcing, and human-driven climate change in establishing this drought and examine the long-term trends that provide the context.

2. Data, models, and methods

a. Observational and reanalysis data

We use a variety of observational datasets generated by the National Oceanic and Atmospheric Administration (NOAA) for the purpose of monitoring national and global climate variations. For precipitation over North America we used the NOAA Climate Prediction Center (CPC) Unified dataset gridded at 0.5° resolution provided by the NOAA Office of Atmospheric Research Earth System Research Laboratory Physical Sciences Division, Boulder, Colorado, and obtained from the International Research Institute for Climate and Society (IRI) at http://iridl.ldeo.columbia.edu/SOURCES/.NOAA/.NCEP/.CPC/.UNIFIED_PRCP/.GAUGE_BASED/.GLOBAL/.v1p0/index.html (Chen et al. 2008). For surface air temperature over North America we use the NOAA CPC Climate Anomaly Monitoring System (CAMS) data gridded at 2° resolution and obtained from the IRI at http://iridl.ldeo.columbia.edu/SOURCES/.NOAA/.NCEP/.CPC/.CAMS/.anomaly/ (Ropelewski et al. 1985). For global precipitation we use the CPC Merged Analysis of Precipitation (CMAP), which combines five satellite-based estimates with gauge observations (Xie and Arkin 1996, 1997). For geopotential heights and SST, we use data from the NOAA National Centers for Environmental Prediction and National Center for Atmospheric Research (NCEP–NCAR) reanalysis obtained from the IRI at http://iridl.ldeo.columbia.edu/expert/SOURCES/.NOAA/.NCEP-NCAR/.CDAS-1/.MONTHLY/ (Kalnay et al. 1996; Kistler et al. 2001). The NCEP–NCAR reanalysis is used here to be consistent with our other related work that takes a longer-term perspective on North American drought (e.g., Seager et al. 2014a, 2017). Results were found to be essentially the same using the more recent NCEP–Department of Energy Reanalysis II (Kanamitsu et al. 2002), which only covers the post-1979 period. We also use the Niño-3.4 SST index (SST anomaly averaged over 5°S–5°N, 170°–120°W) and the Pacific decadal oscillation (PDO) index taken from the NOAA National Centers for Environmental Information (at https://www.ncei.noaa.gov/access/monitoring/pdo/), which follows the PDO index of Mantua et al. (1997) and is based on the leading principal component of monthly Pacific SST anomalies, with global mean removed, north of 20°N. All data used cover the period from January 1979 to May 2021.

b. SST-forced and radiatively forced models

Atmosphere models forced by observed SSTs are used to assess how drought onset is influenced by SST anomalies in the world's oceans. We use ensembles of simulations from three models created for community use by NCAR. For each model, each ensemble member is initialized with a different initial condition but then forced by a common SST dataset. The first model is NCAR Community Climate Model 3 (CCM3; Kiehl et al. 1998) run at the Lamont Doherty Earth Observatory (LDEO) of Columbia University with a spectral dynamical core and triangular truncation at zonal wavenumber 42 (approximately 2.8° at the equator). CCM3 is forced by the HadISST SSTs from the United Kingdom Meteorological Office's Hadley Centre (Kennedy et al. 2011a,b) and data are available at http://kage.ldeo.columbia.edu:81/expert/SOURCES/LDEO/.ClimateGroup/.MODELS/.CCM3/.PROJECTS/.goga/. CCM3 has been our workhorse model for studying North America drought (see Seager et al. 2005). The second model is a low-resolution (2° × 2°) version of the current NCAR

Community Atmosphere Model 6 (CAM6-LR; CAM team 2021; Bogenschutz et al. 2018), run in "-chem none" mode, which disables prognostic aerosols, that was modified and set up by us at LDEO. CAM6-LR was forced by the Hadley blended SST data of Hurrell et al. (2008) and is available at http://hodges.ldeo.columbia.edu:81/expert/SOURCES/.CAM6/.forRichard/.CAM6/.runs/. This model version was created to be more computationally efficient than the standard version and allows us to generate large ensembles of projections for an ongoing NOAA-funded project, which these simulations are part of. The third model is the standard medium-resolution (1°× 1°) CAM6 run by NCAR, denoted CAM6-MR, which is forced by NOAA ERSSTv5 SST data (Huang et al. 2017) and available at https://www.cesm.ucar.edu/working_groups/CVC/simulations/cam6-prescribed_sst.html. There are 16 ensemble members for CCM3 and CAM6-LR and 10 for CAM6-MR. The climate simulated by each ensemble member contains a forced component common to all and internal variability that is uncorrelated across the ensemble members. The ensemble mean isolates the forced component. In the case of CCM3 the only forcing is the SST but for CAM6-LR and CAM6-MR the models are forced by both the SST history and the history of trace gases. In this case the ensemble mean isolates the SST plus trace gas–forced component but we expect this to be dominated by the SST-forced component.

For radiatively forced coupled climate models we use the latest simulations from CMIP6 up to 2018 using the historical simulations extended with the Shared Socioeconomic Pathway 8.5 (SSP-585) (Eyring et al. 2016) through May 2021. Data were obtained from https://esgf-node.llnl.gov/search/cmip6/. We analyze all runs from all models with the necessary data, which provides 45 models and 249 runs (Table 1 in the online supplemental material provides information and citations and data sources for the CMIP6 models). To determine the radiatively forced response we average across ensemble members for each model and then average the ensemble means of all models.

c. Methods

For southwest North America, we use an area-weighted average across the entire Southwest (30°–40°N, Pacific coast to 105°W, marked in Fig. 1). The analysis is also based on four seasons defined as June–August (JJA; summer), September–November (SON; fall), December–February (DJF; winter), and March–May (MAM; spring). For time series of any data, trends were estimated using linear least squares regression with significance assigned at the 95% confidence level according to a two-sided t test. Pearson correlations between the observed and model mean are listed in the legend with significant correlations marked in boldface. To show statistical distributions across years in observations and across ensemble members, or ensemble members and years, in models we use box-and-whisker diagrams. The box encloses the 25th and 75th percentiles of the distribution, the whiskers show the normal distribution range, the middle horizontal line shows the median, and outliers beyond the normal distribution range are shown as circles. To quantify the level of agreement between observed and modeled patterns of geopotential heights we use an area-weighted pattern correlation coefficient (Wilks 1995). For the CMIP6 multimodel-mean trends, we show robustness of results by marking where the multimodel-mean trend is significant at the 95% confidence level and also where three-quarters of model ensemble means agree on the sign of the trend and agree with the sign of the multimodel-mean trend.

3. Results

a. Drought onset in 2020 to 2021 across the Southwest and large-scale atmosphere–ocean context

In Figs. 2a–d we show the time series from March 1979 to May 2021 of observed precipitation over southwest North America. For each season, the last data point is within the drought of 2020 to 2021. Focusing on the blue lines that show the NOAA observed data, the extreme dryness of 2020 to 2021 is clear and it was either the driest or among the driest in the 43 years of data. However, only in MAM does this extremely dry season in 2021 appear at the tail end of a statistically significant drying trend over the period since 1979. The lower four panels in Fig. 2 show the observed surface air temperature time series also with blue lines. There has been a warming trend in the Southwest in all seasons of about 1°C over the last 43 years, which is statistically significant in JJA and SON. JJA 2020 and SON 2020 were among the warmest few summers and falls in this record.

To examine the large-scale context of this run of extreme dry seasons in 2020 to 2021 in the Southwest, in Fig. 3 we plot the anomalies in each season of NOAA CPC precipitation over land, SST over the ocean, and 200-hPa heights (left column) and NOAA CMAP satellite-gauge precipitation over land and sea and 700-hPa heights (right column) for the equatorial and Northern Hemisphere domain. First of all, looking at the precipitation it is seen that the dry conditions in the Southwest were part of a low precipitation anomaly that, in all four seasons, extended across the North Pacific Ocean and into North America. Also, in all four seasons, there are dry anomalies across the entire equatorial Pacific Ocean. The reasons for that are clear in the maps of the SST anomaly, which show that cold anomalies formed in JJA 2020 (Fig. 3a) in the central to eastern equatorial Pacific, intensified in SON 2020 (Fig. 3c), and spread west across almost the entire equatorial Pacific, strengthening in the west Pacific in DJF 2020/21 (Fig. 3e) but weakening in the east and dissipating in MAM 2021 (Fig. 3g). Hence the drought onset was concurrent with the development, intensification, and weakening of a La Niña event.

Seager et al. (2014a) show La Niña composites of circulation anomalies by season. In summer the composite circulation anomalies are very weak but coherent circulation anomalies span the Northern Hemisphere from fall to spring. The circulation signal of a La Niña in these seasons is typically low upper-troposphere heights in the tropics with twin cyclones straddling the equator above and to the west of the anomalous negative heat source and, in the Northern Hemisphere, ridges in the subtropics to midlatitudes, an anomalous high over the

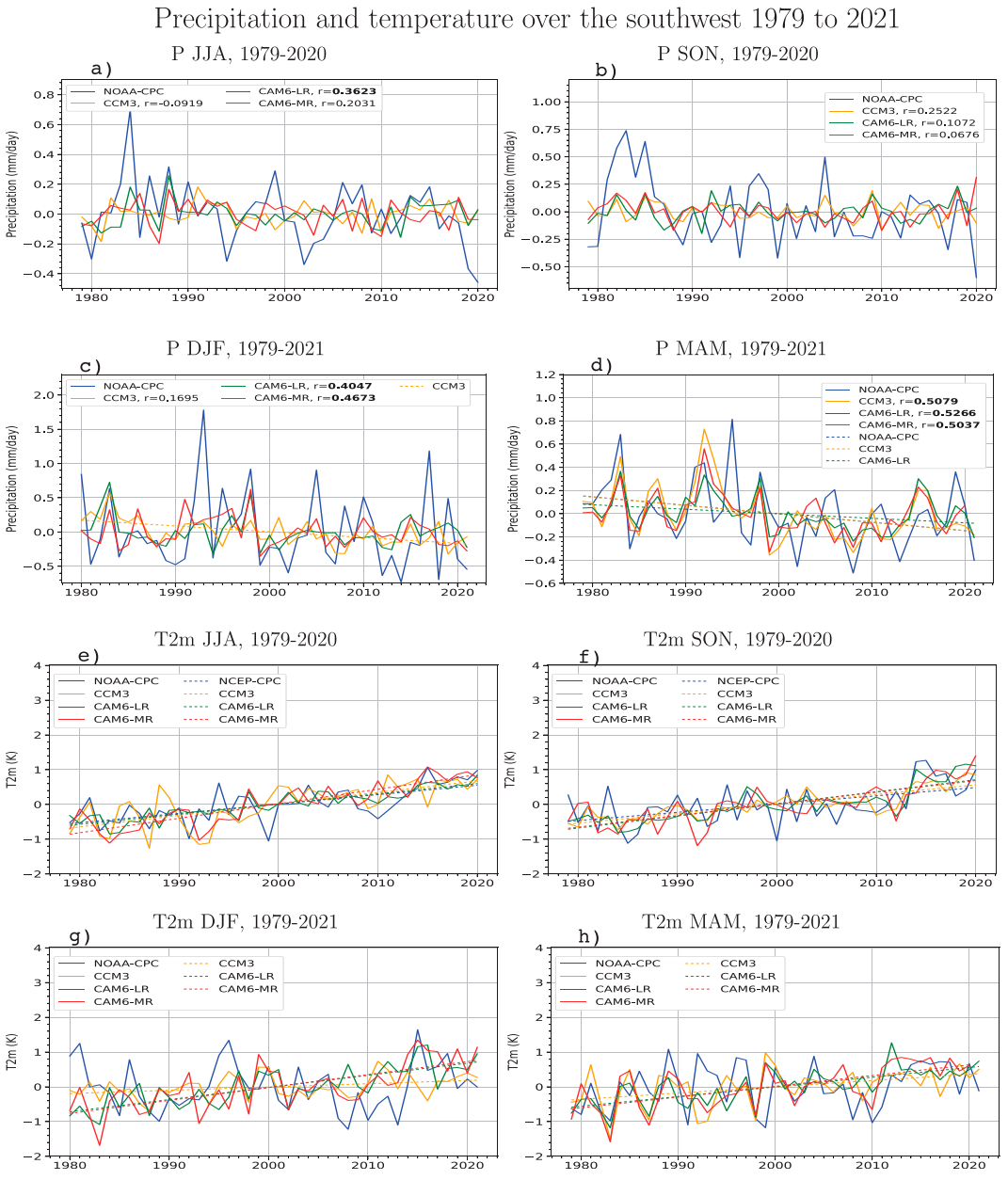

FIG. 2. Time series of (a)–(d) precipitation and (e)–(h) surface air temperature for observations (blue) and the three SST-forced atmosphere models for four seasons as indicated by panel headings. Linear trends are shown where significant at the 95% confidence level.

North Pacific, and an anomalous low over Canada (e.g., Lau et al. 2005; Seager et al. 2014a; Okumura et al. 2017). Despite the appearance of cold eastern equatorial Pacific SSTs in JJA 2020, consistent with Seager et al. (2014a) and Kumar and Hoerling (1998), the Northern Hemisphere circulation did not show any canonical evidence of tropical forcing, in agreement with tropics-to-extratropics teleconnections being weak in the summer (Kumar and Hoerling 1998). Instead there was a high anomaly between 20° and 50°N over the North Pacific in the upper troposphere, which would lead to descending air over western North America (Fig. 3a). This high is also present, but weaker, at 700 hPa (Fig. 3b). However, these seasonal mean circulation anomalies do not appear particularly strong or readily able to explain the exceedingly dry conditions in summer 2020, a matter we return to later.

In SON 2020 a typical La Niña circulation pattern for the cooler seasons appears with a ridge stretching across the North Pacific, the United States, and Mexico and into the midlatitude Atlantic. This went along with reduced precipitation over Mexico and the western to central United States (Figs. 3c,d). In DJF 2020/21 and MAM 2021 (Figs. 3e–h) there was also a high over the North Pacific that extended to western North

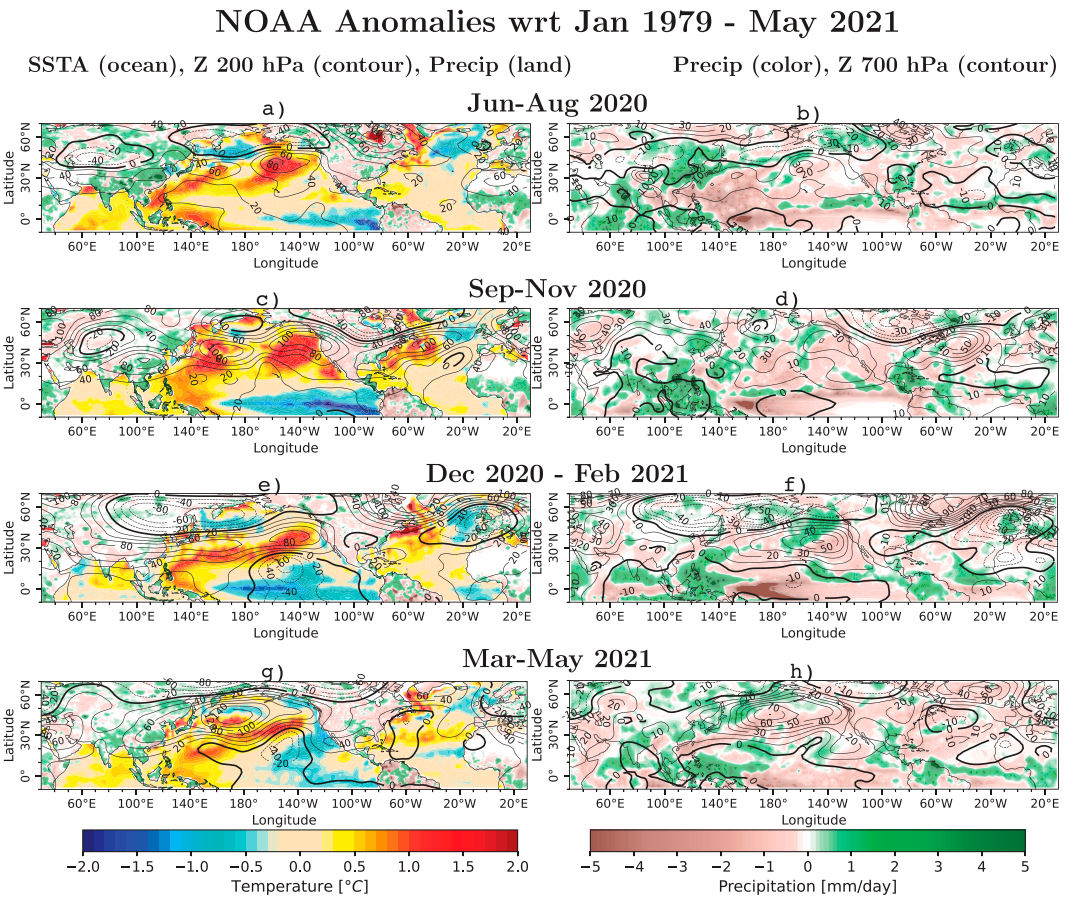

FIG. 3. The large-scale atmosphere–ocean context of the 2020/21 drought onset. Maps show (left) the anomalies of SST (ocean) (colors; K), CPC precipitation (land) (colors; mm day^{-1}), and 200-hPa heights (contours; m) and (right) CMAP precipitation (colors; mm day^{-1}) and 700-hPa heights (contours; m) for (from top to bottom) JJA 2020 through MAM 2021.

America where precipitation was low. In these seasons the cyclone north of the equator in the tropical Pacific was associated with reduced diabatic heating and reduced precipitation (Figs. 3f,h). The 700-hPa heights (Figs. 3b,d,f,h) show that the extratropical circulation anomalies are coherent from the upper to lower troposphere in all seasons, including summer. The similarity of the height anomalies in fall 2020 through spring 2021 to the La Niña composites in Seager et al. (2014a) suggests a role for tropical SST driving of the drought evolution in these seasons.

b. *Climatological configuration of precipitation and circulation in the West*

The drought has impacted the entire Southwest, encompassing regions with different climates and seasonality of precipitation. To illustrate this, Fig. 4 shows maps of climatological land precipitation and 700-hPa heights and winds for JJA, SON, DJF, and MAM (Figs. 4a–d) as well as monthly climatological time series of precipitation for coastal (coast to 117°W) and central (117°–105°W) subdivisions of the Southwest region between 30–40°N as shown in (Figs. 1 and 4e,f). The coastal portion of the Southwest receives maximum precipitation in midwinter related to strong onshore westerly flow and is almost totally dry in the summer, typical of a Mediterranean-type climate (Seager et al. 2019b). The interior West, by contrast, receives maximum precipitation in summer and is drier in spring and fall, but also has a weaker precipitation maximum in winter. The summer precipitation maximum is related to southwesterly flow that can draw moisture from the southeast tropical Pacific and southeasterly curving to southwesterly flow that can draw moisture from the Caribbean and Gulf of Mexico. Of the three SST-forced models, CCM3 notably fails to simulate the summer interior precipitation maximum (Figs. 4h,j,l). For a drought to impact the entire Southwest throughout the year requires cool season circulation anomalies that have the potential to impact the whole region and warm season circulation anomalies that impact the interior.

c. *Time evolution over 2020 to May 2021 of drought in the coastal and interior West*

Figures 4e–l also show the time series of precipitation for the coastal and interior boxes from January 2020 to May 2021.

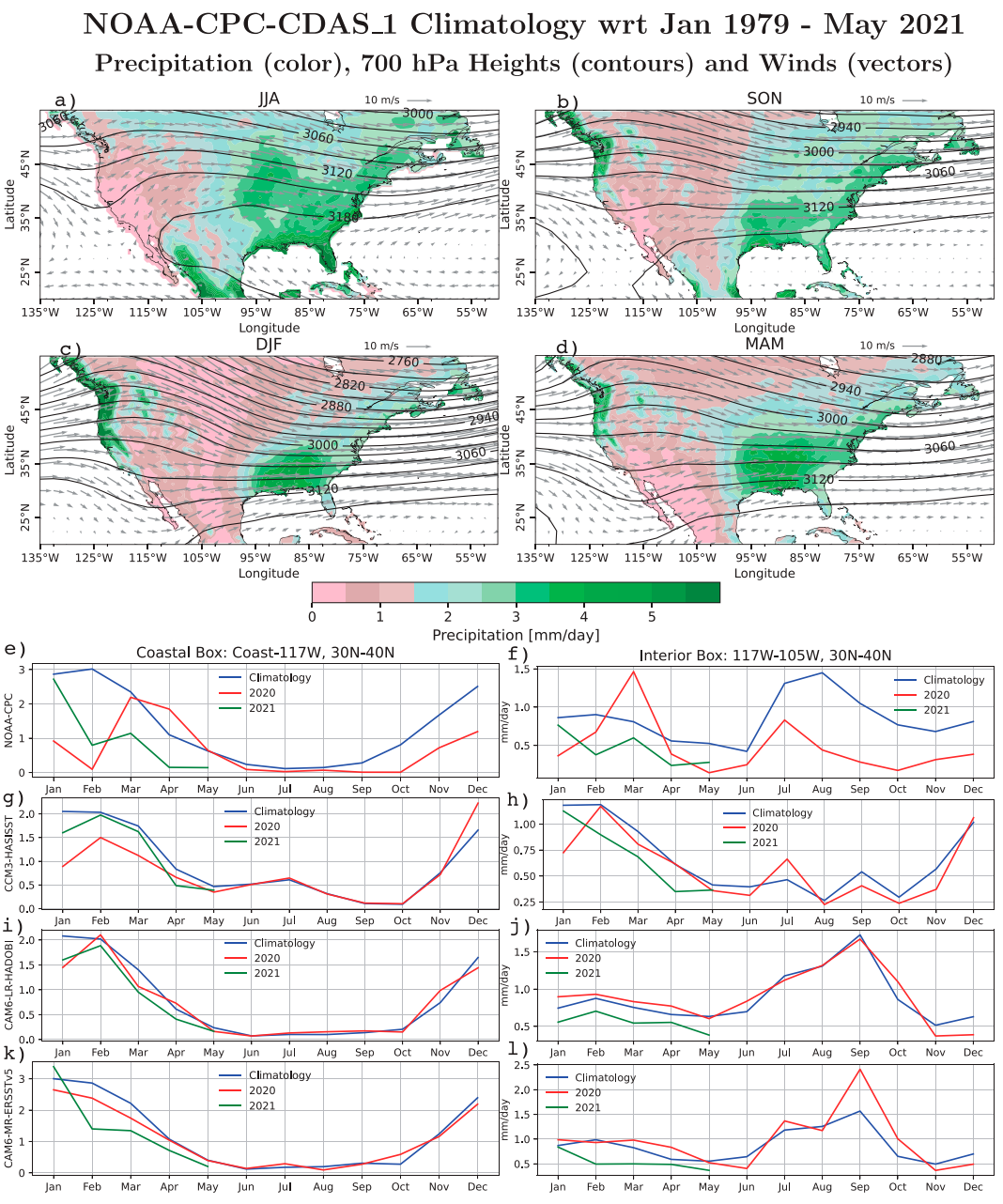

FIG. 4. The climatological observed precipitation (land) (colors; mm day^{-1}) and reanalysis 700-hPa heights (contours; m) and winds (vectors; m s^{-1} with a reference vector at the top right of each panel) for the (a) JJA, (b) SON, (c) DJF, and (d) MAM seasons. Also shown are the climatological precipitation (blue line), the 2020 precipitation (red line), and January–May 2021 precipitation (green line) for (e),(f) observations and the (g),(h) CCM3, (i),(j) CAM6-LR, and (k),(l) CAM6-MR SST-forced models, for the (left) coastal and (right) interior subregions. Precipitation units are mm day^{-1}.

In the coastal region, midwinter 2020 was dry followed by a normal spring and then fall, winter and spring were dry, interrupted by a near-normal January in 2021. Notably in February 2021 the region received only one-third of normal precipitation and the wet season ended early with only half the normal precipitation in March 2021. In the interior, after a very wet March 2020 every month through to May 2021 was drier than normal and the deficits in August and September 2020 were particularly striking. As will be examined in detail later, the three SST-forced models fail to simulate the dry summer in 2020 in the interior but suggest some ability to simulate drier than normal conditions in winter/spring 2021 (Figs. 4h,j,l). All three SST-forced models simulate drier than normal conditions in the coastal region in January to April 2021 although less than observed (Figs. 4g,i,k).

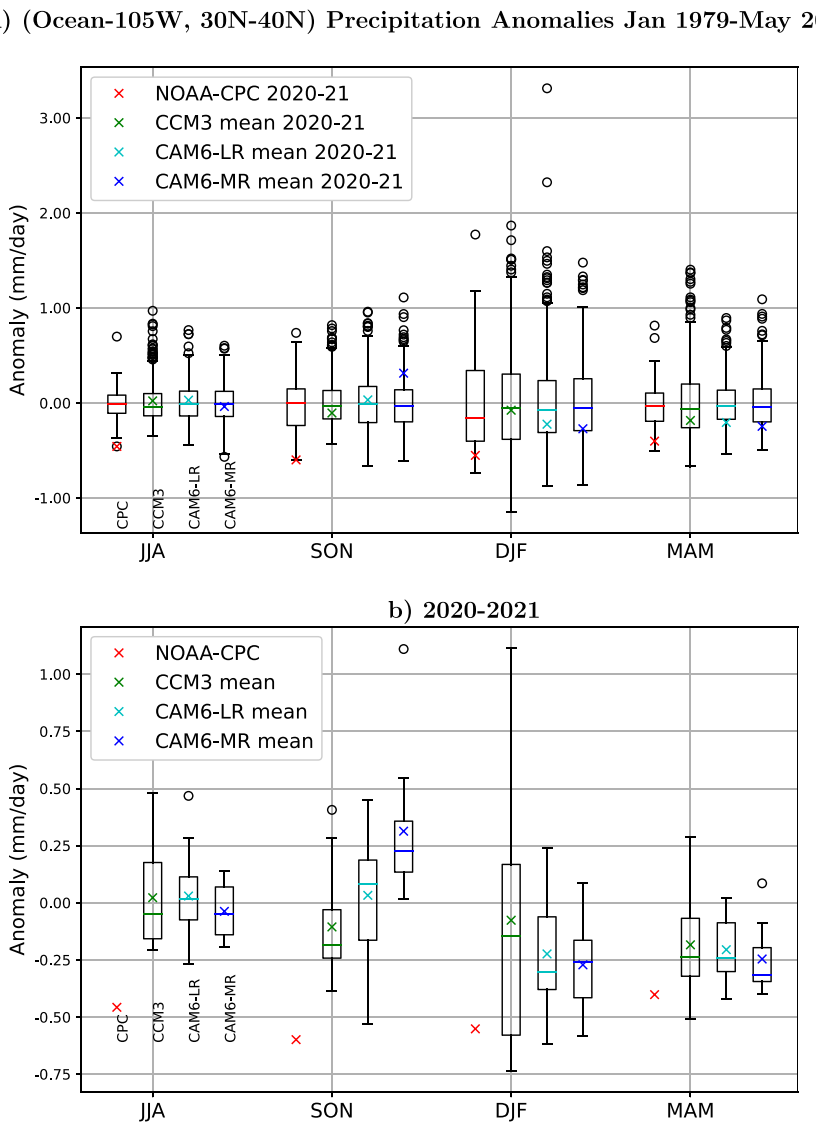

FIG. 5. Box-and-whisker plots showing the distribution of precipitation anomalies in observations and three SST-forced models area-weighted and averaged over the Southwest drought region. (a) Distributions across all seasons and, for models, all seasons and ensemble members. (b) Distributions for just the 2020–21 drought seasons for which the observed values are just the single red crosses. The box shows the 25th–75th-percentile range of the distribution, the whiskers indicate the range, the horizontal line shows the median, and the cross is the mean, with outliers shown as circles. Units are mm day^{-1}.

d. Using simulations with SST-forced models to examine the role of ocean driving of drought onset and evolution

1) PRECIPITATION SIMULATIONS

The SST-forced ensembles provide a useful model-based estimate of the roles of ocean forcing and internal atmosphere variability in generating the drought onset and subsequent evolution. The ensemble mean for each model provides an estimate of the response to SST forcing that is common to each ensemble member. The spread of ensemble members around the ensemble mean provides the model's internal atmosphere variability. For the observations, with the limited data available, we can estimate the total variability by looking at the spread of precipitation anomalies across years for a given season.

Figure 5a shows the seasonal precipitation anomalies for the entire Southwest box. Given the knowledge of the seasonal distribution of precipitation across the Southwest, the winter anomalies will be reflective of those in the coastal region and the summer anomalies of those in the interior region. Shown are the cross-year spread for observations and cross-year

and cross-ensemble members spread for each of the three SST-forced models.

For the observations, JJA 2020 was the driest summer in this period (see also Hoell et al. 2022). It was followed by three consecutive seasons with abnormally dry conditions even though each was not the driest on record. Such a four-season string of dry conditions would be highly unlikely if precipitation in each season was uncorrelated with that in other seasons. While land surface feedbacks can provide some persistence, if SST driving was important, given the season-to-season persistence of SST anomalies, then such persistence of precipitation anomalies across seasons might be less surprising.

Turning to the SST-forced models, they collectively well simulate the observed variability of seasonal mean precipitation in each season in the Southwest. The model spread is, as expected, higher than that in observations given the larger sample size enabled by the model ensemble versus the single realization in nature. Despite this larger spread, the models confirm that the observed dry conditions in all four seasons were quite extreme: they are near the dry limit of what these three climate models can simulate and, for JJA 2020, only one model (CAM6-MR) has a JJA more extreme than that observed. In Fig. 5a the model ensemble means for the seasons from JJA 2020 to MAM 2021 are shown by colored crosses within each box plot. For JJA 2020, these ensemble means scatter around zero and hence provide no evidence that the extreme dry conditions in summer that initiated the drought were driven by ocean conditions. Similarly, for SON 2020 the models provide no collective evidence that ocean driving was responsible for the intensification of the drought. By contrast, for DJF 2020/21 and MAM 2021 the models provide strong evidence that continued drought intensification was driven by ocean conditions. However, even though the ensemble-mean precipitation anomalies in these two seasons hovered in the lower tercile, they were still much wetter than observed.

In Fig. 5b, we show the box-and-whisker plots for the model ensemble spreads for the simulations of just the 2020–21 seasons together with the single observational value for the seasons. Clearly, SST-driving did shift the ensemble of precipitation simulations in DJF 2020/21 and MAM 2021 in the dry direction so that the entire 25th–75th percentiles of the distribution were drier than normal and some ensemble members of CCM3 and CAM6-LR were drier than the observations. As such the dry conditions in these two seasons can be explained, in the context of these models, in terms of a combined effect of ocean conditions providing a shift toward drier conditions and internal atmosphere variability working in the same direction. This is not surprising given the extremity of the drying. For JJA and SON 2020, the model ensembles are not shifted dry and the observations are outside the ensemble range of simulations of that particular season although less so, or within, the range of simulations of all JJA and SON seasons (Fig. 5a).

2) CIRCULATION SIMULATIONS

It is also necessary to assess how well the SST-forced models reproduce the circulation anomalies within which the drought onset was embedded. For example, the models might simulate the circulation anomaly reasonably but fail to simulate the associated precipitation anomalies over North America. To that end, Fig. 6 shows the hemispheric precipitation and 200-hPa height anomalies for the JJA 2020 through MAM 2021 seasons as seen in the ensemble means of the three SST-forced models. These should be compared to Fig. 3. First of all, each of the models simulates dry anomalies along the equatorial Pacific that track the cold SST anomaly in amplitude and longitudinal location from JJA 2020 to MAM 2021. As we already noted, the observed seasonal mean circulation anomaly in JJA 2020 (Figs. 3a,b) was indistinct in terms of its ability to drive drought over the Southwest. It did have a midlatitude ridge stretching from the Arabian Peninsula across Asia and the Pacific to the North American west coast and another high over Hudson Bay. Each of the models also generates a midlatitude ridge but in different latitudes and with centers at different longitudes and with little agreement with the observations (Figs. 6a–c). We discuss JJA 2020 more below. Moving on to SON 2020 (Figs. 6d–f), there is notably more agreement between observed and modeled Northern Hemispheric circulation anomalies: the circumpolar ridge with centers over the western and eastern North Pacific and over the northwest Atlantic is seen in observations (Figs. 3c,d) and the two CAM6 models, while CCM3 differs in having a single North Pacific high. However, in the observations, the east Pacific high is located to provide northerly (and descending) flow over western North America but only CAM6-LR does this and then weakly so. Hence, given these circulation anomaly differences, it is not surprising that the models underestimate the SON 2020 drying. However, the agreement does suggest that there was an SST-driven component to the flow anomalies in this season of the drought, and perhaps therefore to the drying too, even though the models miss that crucial detail.

For DJF 2020/21 and MAM 2021 (Figs. 6g–l) all three model ensemble means have the classic signal of La Niña forcing in the tropics and in the midlatitudes: twin cyclones straddling the equatorial Pacific and an anomalous high over the North Pacific that stretches across southern North America to the Atlantic Ocean. The Pacific features are similar to those observed (Figs. 3e–h) but the observed high does not extend east to the Atlantic. Nonetheless, it is the northerly component of flow on the eastern flank of the anomalous North Pacific high that induces drying and the models capture drying in the same location due to the placement of anomalous highs. Hence the models support the idea that the drought evolution in winter and spring was guided by a classic La Niña teleconnection. The pattern correlations between the observed and modeled height anomalies are strongest in spring 2021, suggesting that this is the season in which the ocean driving was most effective.

e. A closer look at summer 2020

The seasonal maps for JJA 2020 did not show an obvious drought-inducing circulation anomaly over western North America. To understand what caused the drought onset in this season, in Fig. 7 we show North American close-ups of

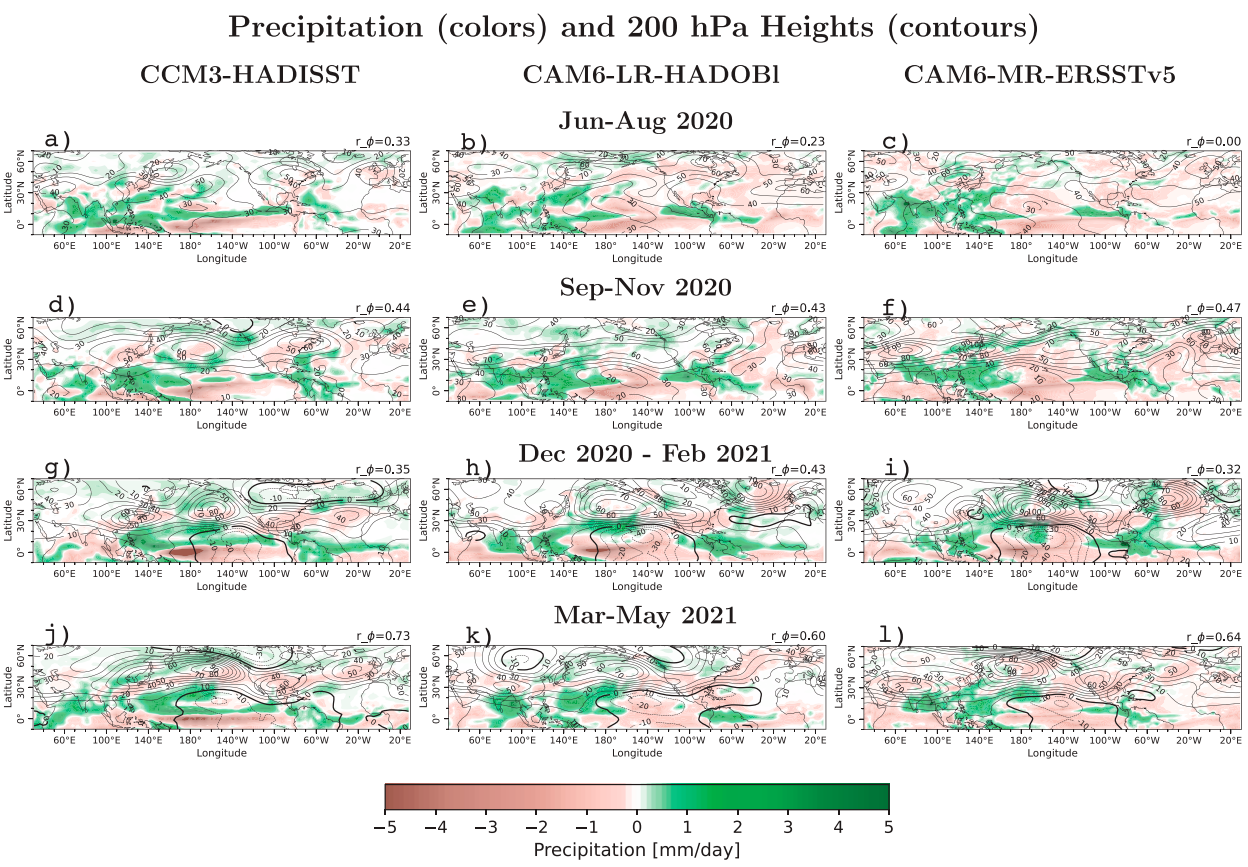

FIG. 6. Large-scale atmosphere–ocean context of the drought onset in simulations from the (left) CCM3, (center) CAM6-LR, and (right) CAM6-MR SST-forced models for (a)–(c) JJA 2020, (d)–(f) SON 2020, (g)–(i) DJF 2020/21, and (j)–(l) MAM 2021. Shown are precipitation anomalies in colors (mm day^{-1}) and 200-hPa height anomalies in contours (m). The pattern correlation between the observed and modeled height anomaly across the domain is shown to the upper right of each panel.

the 700-hPa circulation and precipitation anomaly for each month from June through September 2020. In June 2020 (Fig. 7a), a complex of small-scale circulation anomalies did lead to modestly dry conditions across the Southwest; in July 2020 (Fig. 7b) there were also scattered but weak negative precipitation anomalies across the Southwest. In contrast, in August 2020 (Fig. 7c) there was a large high pressure anomaly over California and the Gulf of California and a deep low over the Mississippi valley to the east. These pressure systems established strong northerly flow from Canada to southern Mexico across the Southwest. This flow would have effectively hindered moisture flow into the southwest from both the Gulf of California and the Gulf of Mexico and, consistently, was associated with widespread dry conditions. This circulation feature actually persisted in September 2020 and even strengthened (Fig. 7d) and explains why precipitation in these 2 months was only about a third of normal (Figs. 4e,f). This key subseasonal-time-scale anomaly was obscured in the JJA seasonal mean. Although not shown here, none of the SST-forced models produced these subseasonal circulation features. Furthermore, while the August and September 2020 circulation anomalies were similar over North America, they were embedded within quite different hemispheric patterns. In August there was a zonally extended north–south trough–ridge pattern from Asia to North America whereas in September there was a circumpolar Rossby wave with a prominent arching structure from subtropical Asia to the Bering Sea and then to the North American West Coast.

f. What is the role of climate change? Long-term trends in precipitation and temperature

1) PRECIPITATION–TEMPERATURE RELATIONSHIPS DURING SUMMER IN THE INTERIOR WEST

Southwestern North America has warmed over the study period (1979–2021) as seen in Fig. 2 and, according to this data, this is significant in summer and fall. However, surface air temperature also responds to drought. It might be expected for purely meteorological reasons that droughts associated with high pressure would also be warm due to, for example, subsidence and less cloud cover. However, beyond that, in water-limited areas, drying soils lead to a repartitioning of the surface energy budget from latent cooling to sensible and longwave cooling requiring an enhanced surface temperature (e.g., Hoerling et al. 2013; Koster et al. 2009; Yin et al. 2014; Cheng et al. 2019; McKinnon et al. 2021). Indeed,

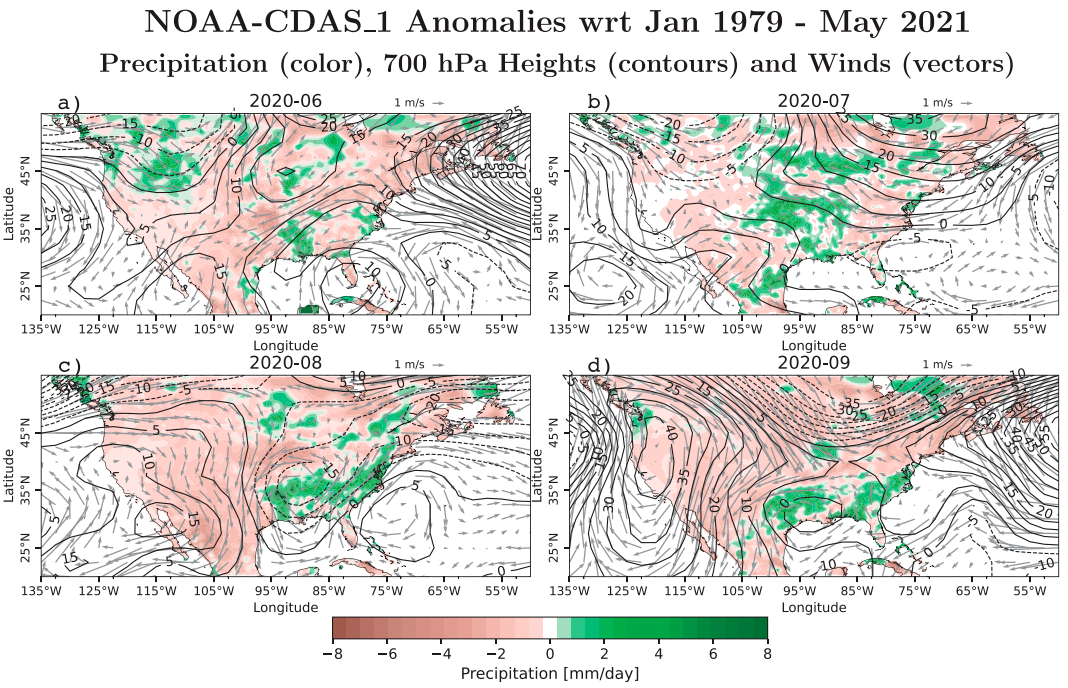

FIG. 7. Observed precipitation (land) (colors) and reanalysis 700-hPa heights (contours) and winds (vectors) anomalies for (a) June (b) July, (c) August, and (d) September 2020. Units are mm day^{-1} for precipitation, m for heights and m s^{-1} for wind with reference vector at the top right of each panel.

Berg et al. (2014) show how interactive soil moisture in a climate model enhances variance of summer surface air temperature including over western and central North America. To look into this for our case, in Fig. 8 we plot temperature anomalies against precipitation anomalies for each year for the JJA summer season and just for the interior Southwest region. We focus on the summer interior, where and when moisture supply is most limited, because this is where we expect to possibly see evidence of a drought–heat relationship. For the observations (Fig. 8a) the 2020 JJA season clearly stands out as the driest on record and also, by a smaller margin, the hottest on record. The years are color-coded and the warming over the time period (over 1°C) is obvious but 2020 does not stand apart from the general warming trend. The scatter of points hints at a tendency for drier years to be warmer, according to the physics of droughts and heat waves as the above references discuss, but this relationship in this location and season is weak. It also was not any stronger when the precipitation time period was expanded to March–August to allow for soil moisture memory and a delayed effect on summer temperature.

The observed precipitation anomaly in JJA 2020 is clearly out of range of the CCM3 model (Fig. 8b) but, according to both versions of CAM6 (Figs. 8c,d), is attainable but exceedingly rare. For all three models the observed temperature anomaly of JJA 2020 is easily attainable but made much more likely by the steady warming trend over the past few decades. The scatter of ensemble members for JJA 2020 (red crosses in Figs. 8b–d) again confirms the lack of a tendency to dry conditions arising from SST forcing. The two CAM6 models, especially the MR version, support the existence of a weak negative correlation between surface air temperature and precipitation, according to established drought physics. For both CAM6 versions, the observed JJA precipitation and temperature anomalies can be explained in terms of this relationship and do not require extraordinary explanations for their occurrence.

2) TRENDS IN OBSERVED AND SST- AND RADIATIVELY FORCED MODEL PRECIPITATION AND TEMPERATURE OVER 1979–2021

To assess if the observed trends in precipitation and temperature can be explained in terms of SST and/or radiative forcing in Fig. 9 we show box-and-whisker plots of the 1979–2021 trends by season from each of the three SST-forced model ensembles and the CMIP6 ensemble. The single observed value for each season is also shown and is enclosed within a diamond if significant at the 95% confidence level. The observed trend is toward drying in every season (Fig. 9a; see also Fig. 2) but only in MAM is it statistically significant. Looking at Figs. 2a and 2b, it is clear that the drying trends in JJA and SON are highly influenced by wet years at the beginning of the record and the 2020/21 drought in the final year. In contrast, and consistent with its significance, the drying in MAM (Fig. 2d) arises from a steadier drying or a shift at the turn of the century to a drier climate.

For JJA and SON precipitation none of the SST-forced or radiatively forced models provide evidence of a drying trend. However, for DJF and MAM the SST-forced models provide evidence of SST-driven drying, and CCM3 can readily match

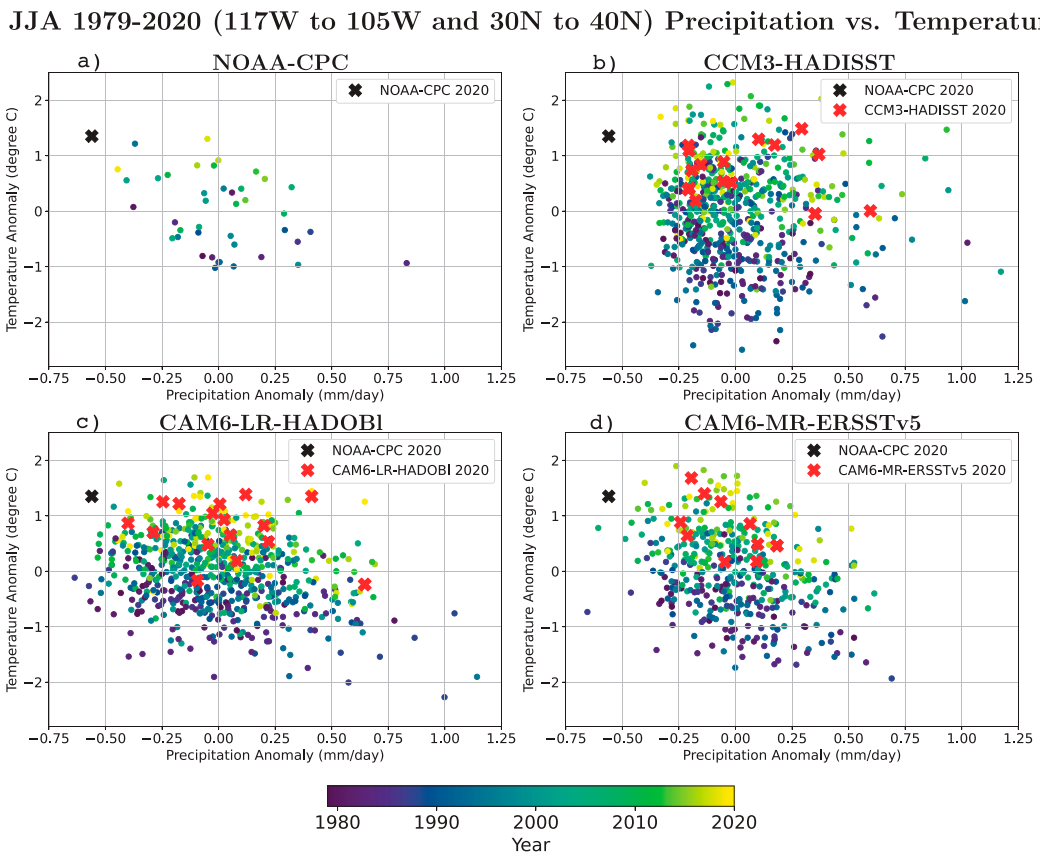

FIG. 8. The relationship between surface air temperature and precipitation anomalies in the interior Southwest during summer for (a) observations, where each dot represents one summer, and (b)–(d) the models as labeled, where each dot represents an ensemble-member simulation for a season. The dots are colored according to the year to which the data refers (see color bar at bottom).

the amplitude of the observed drying trend. In contrast, the CMIP6 models provide no evidence of a radiatively driven drying trend and most members do not dry as much as the observations.

The observed warming trend is significant in JJA and SON but not in DJF or MAM (Fig. 9b). The CMIP6 models tend to greatly overestimate the warming in all seasons while the SST-forced models are more in line with observed warming though still on the too-warm side, and especially so in DJF except for CCM3.

To place these area-averaged trends in a spatial context, in Fig. 10 we show maps of the observed and CMIP6 multimodel-mean precipitation trend over 1979–2021. The observed trends are marked where significant at the 95% confidence level. The CMIP6 trend is stippled where the ensemble-mean trend is significant at the 95% confidence level and hatched where three-quarters of models agree on the sign of the change and with the sign of the ensemble-mean change. As expected, the observed trends, which contain the full value of any trends introduced by internal climate variability, are often much larger than the CMIP6 ensemble-mean trends, which for an ensemble as large as this will well isolate the radiatively forced trend by averaging out uncorrelated internal variability in the individual model runs. Despite these differences, there are some noticeable similarities in the spatial patterns of the observed and modeled trends. In JJA there is observed drying across the West that is significant in some locations (Fig. 10a) and the models suggest the Pacific Northwest component of this is radiatively forced (Fig. 10b). In the interior Southwest in JJA the observed drying is significant in some locations but the models do not support it being forced. Interestingly, the models suggest a forced wetting in the core of the monsoon in Mexico and this is also hinted at in observations, though not significant. Western drying, though again mostly not significant, has occurred in SON and again the models do not support this being forced (Figs. 10c,d). In DJF the observed drying in Mexico is supported as forced by the models (Figs. 10e,f). In observations, this drying extends into the southern and western parts of our study area in the United States, but not in models. In MAM, observations and models both show drying in the Southwest, supporting this as a forced response (Figs. 10g,h). (Although outside our study area, the models suggest that the wetting in the Southeast in JJA and the Appalachians in DJF is forced.) The lack of significance in model precipitation trends for the drought region area averages used here, therefore arises in part from the area straddling regions of forced drying and

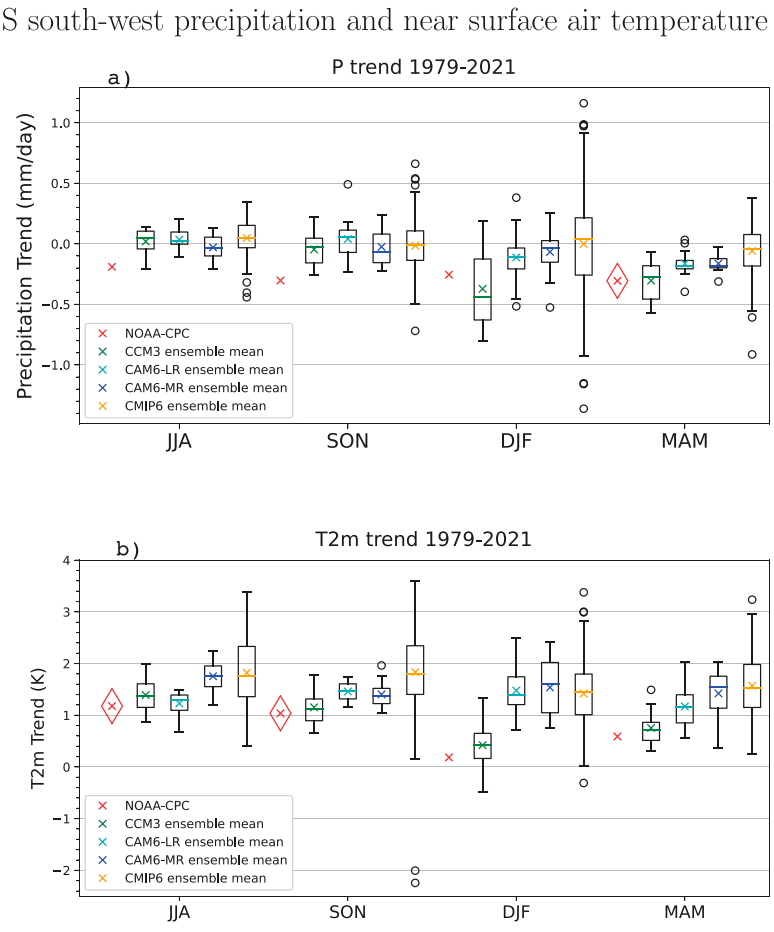

FIG. 9. Box-and-whisker plots for the trends in (a) precipitation and (b) surface air temperature over 1979–2021 for, from left to right, JJA, SON, DJF, and MAM for the CCM3, CAM6-LR and CAM6-MR SST-forced models and the CMIP6 ensemble with observed trends shown as red crosses and enclosed in a diamond if statistically significant. For the box and whiskers, the box encloses the 25th–75th-percentile range of the distribution, the horizontal line in the box is the median, the cross inside the box is the mean, the whiskers show the range, and the circles mark outliers. Units are mm day^{-1} for precipitation and K for temperature change over the 1979–2021 period.

wetting, each with statistical significance concentrated to their south or north.

3) PACIFIC DECADAL VARIABILITY AS A CONTRIBUTOR TO DRYING TRENDS IN THE SOUTHWEST

The SST-forced models suggest that the ocean has driven a drying trend in the Southwest in winter and spring that contributed to making the drought in the last 2 years worse than otherwise. This is almost certainly related to Pacific decadal variability (Zhang et al. 1997; Chen and Wallace 2015) or, as it is often called, the Pacific decadal oscillation (PDO; Mantua et al. 1997; Mantua and Hare 2002; Newman et al. 2016). The PDO is a pan-Pacific mode of natural climate variability that has many similarities in spatial patterns of SST and precipitation to ENSO, and indeed is coupled to ENSO, but which has decadal time scales. The PDO was in a phase in which the tropical Pacific was warm from about 1977 to 1998 and then switched to the phase with a cool tropical Pacific, which has lasted, off and on, ever since. Since the PDO is known to influence precipitation over North America (Huang et al. 2005; Ault and St. George 2010; McAfee 2014; Seager 2015), this should have contributed to the drying trend from 1979 to 2021. While the SST anomalies associated with Pacific decadal variability span the Pacific, it is the tropical component that drives the global response (Seager et al. 2005; Huang et al. 2005), which, consistently, is quite hemispherically symmetric (Garreaud and Battisti 1999; Herweijer and Seager 2008; Seager 2015).

To probe this, we show time series of precipitation in the Southwest, the Niño-3.4 SST and PDO indices, with linear trend lines shown if statistically significant (Fig. 11a) and the linear trend over 1979–2021 of the near-global SST, 200-hPa height and precipitation (Figs. 11b,c), all for the December to

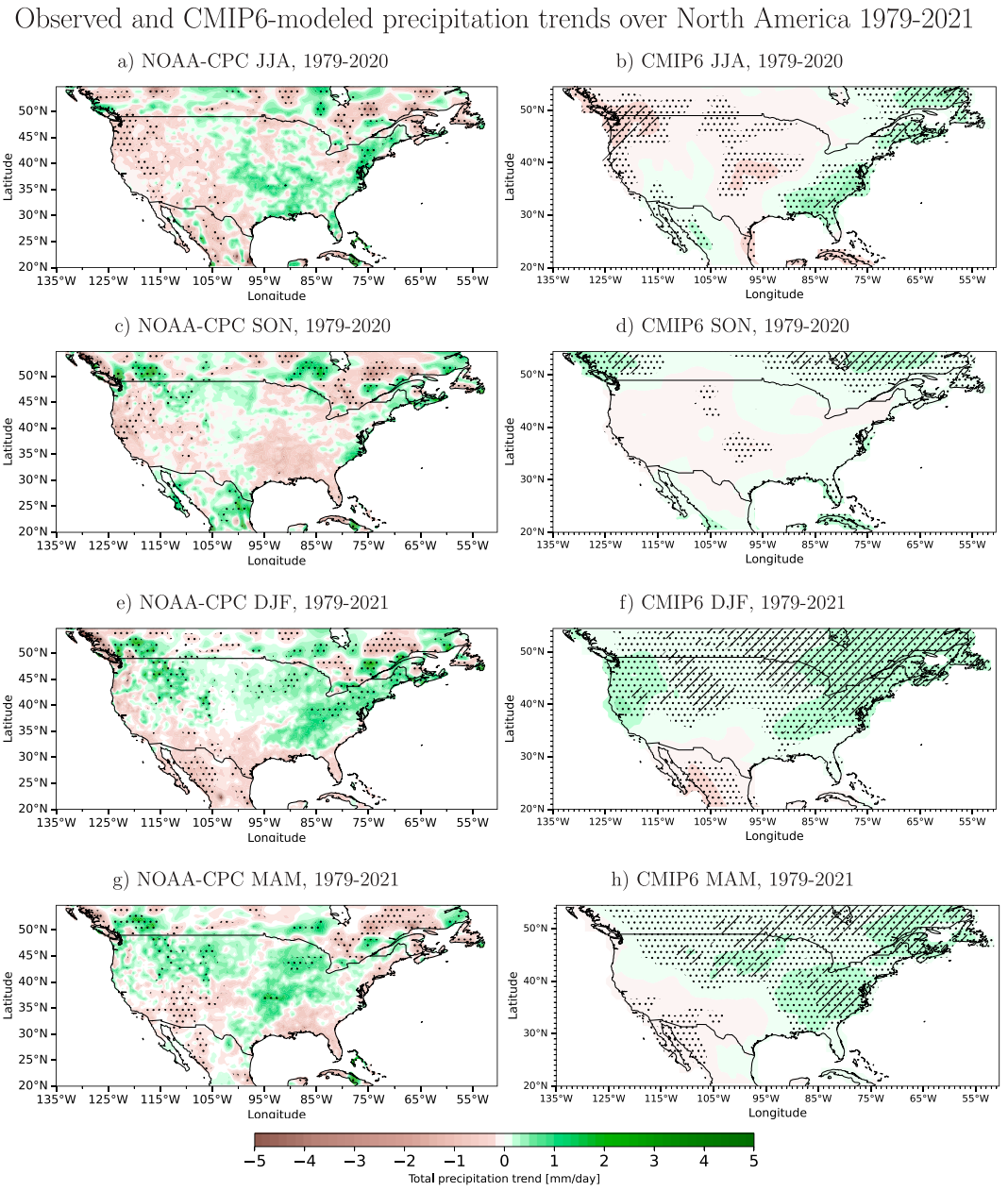

FIG. 10. The (left) observed and (right) CMIP6 multimodel-mean trends in precipitation over 1979 to 2020 or 2021 for (a),(b) JJA, (c),(d) SON, (e),(f) DJF, and (g),(h) MAM. The observed and modeled trends are stippled where significant at the 95% confidence level and the CMIP6 multimodel-mean trend is also hatched where 3/4 of models agree on the sign of the trend and agree with the sign of the trend in the multimodel mean. Units are mm day^{-1} change over the time period.

May half year when we expect the tropical Pacific to be able to influence North American climate. Amidst widespread SST warming, there is cooling in a meridionally broad wedge-shaped region of the central to eastern equatorial Pacific (Fig. 11b). Sitting above this is a region of reduced precipitation and associated off-equatorial anticyclones (Figs. 11b,c), the classic signal of reduced equatorial diabatic heating induced by cold SST anomalies (Gill 1980). This is the signature of a shift to the cool tropics phase of Pacific decadal variability, which is clear in the downward time history of the PDO (Fig. 11a). The tropical heating and circulation anomalies are also teleconnected to a Pacific–North America (PNA)-like pattern with a North Pacific ridge that extends across southern North America (Fig. 11b, see also Lehner et al. 2018) to the Atlantic and a trough over Canada. This decadal trend pattern is actually rather similar to the height anomalies

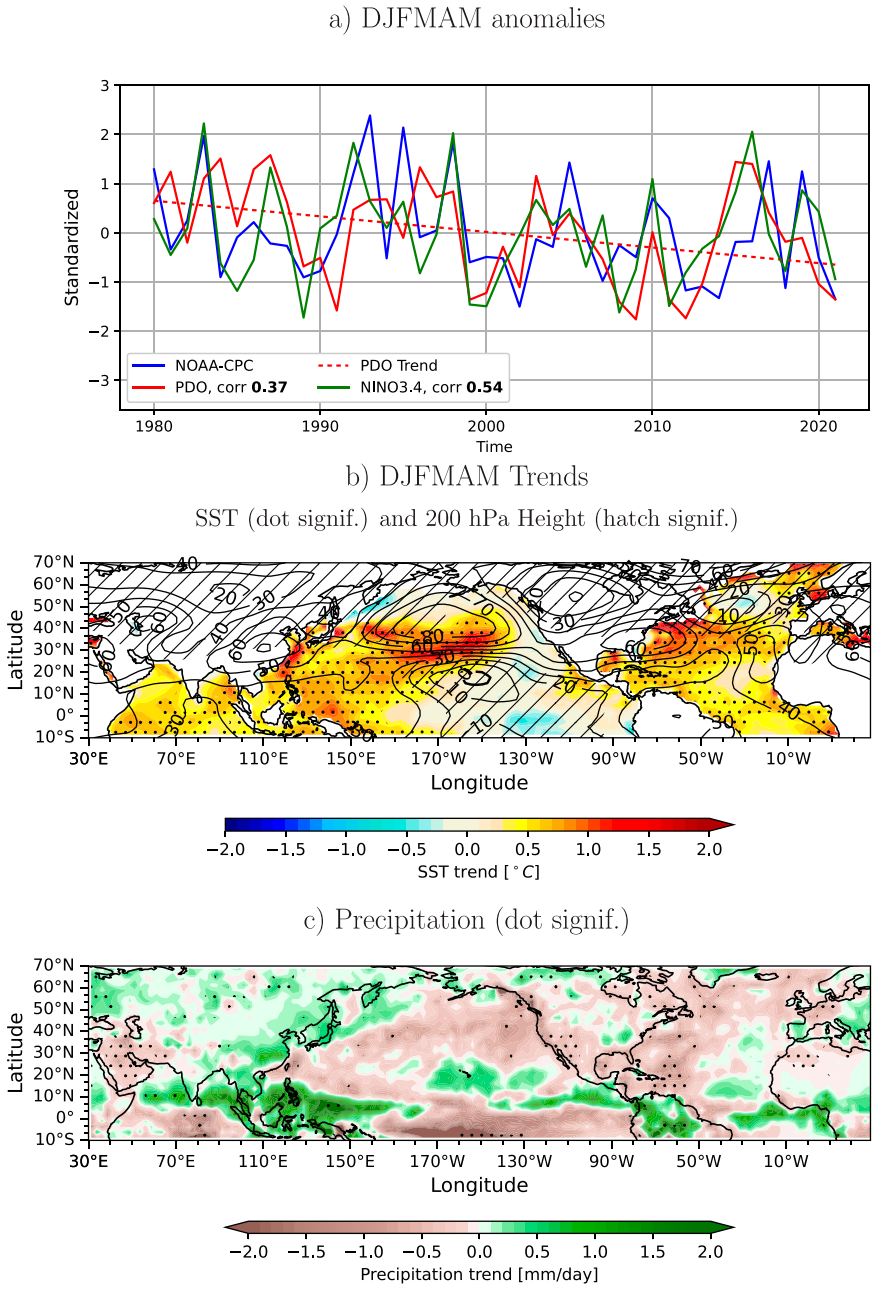

FIG. 11. (a) Time series of the PDO and the Niño-3.4 SST index together with NOAA-CPC precipitation in the Southwest drought region all for the December–May half years over 1979–2021. Correlation coefficients between PDO/Niño-3.4 and precipitation time series are indicated. Trends are shown where significant at the 95% confidence level, which is only for the PDO. (b) Linear trends in SST and 200-hPa height and (c) linear trends in combined satellite–gauge precipitation, all for the December–May half year and 1979–2021. Significance at the 95% confidence level is shown with dots for SST and precipitation and hatching for heights. Units are mm day^{-1} (for precipitation), K day^{-1} (for SST), and m (for heights) for change over the time period.

simulated by the SST-forced models during the 2020/21 La Niña, which testifies to the role of SST forcing in generating these decadal circulation trends. Consistently there is a drying trend in southwest North America although this is only significant in Mexico and the far southwestern United States (Fig. 11c). Notably the trend over this period is only contributing to the drought in the southern portion of the region that went into drought in 2020/21.

4. Conclusions

Here we have studied the physical mechanisms that drove southwestern North America into drought between summer 2020 and spring 2021. We have also placed this drought in the context of longer-term variations, both due to internal natural variability and radiatively forced and human-induced climate change.

The conclusions are as follows:

- The drought onset over summer 2020 to spring 2021 was caused by four consecutive seasons of below-normal precipitation that were either records or at least extreme in the post-1979 period. The drought covered a wide area of the Southwest that included both Mediterranean-type climates at the coast and the semiarid interior and, as such, was driven by reductions in cool-season precipitation, which affected the coastal and interior regions, and warm season precipitation, which only affected the interior.
- The driest summer in the record occurred in 2020 and started the drought. This was dominated by extreme dry conditions in August and appears to be a result of subseasonal internal atmosphere variability since no models simulated SST-induced dry conditions in the season. Fall 2020 dry conditions also appear to have arisen from internal atmospheric variability.
- From winter to spring 2021 the drought was partly driven by La Niña conditions in the tropical Pacific Ocean but the constructive influence of internal atmosphere variability was needed for conditions to become as dry as observed. For all seasons observed dry conditions are just about inside the model range of variability produced by the sum of internal atmosphere variability and SST forcing.
- Over the post-1979 period the PDO has shifted toward its cool tropical Pacific phase. This has favored a shift toward dry conditions in the Southwest focused on the southern part of the recent drought region according to a La Niña–like teleconnection. In all seasons the observed trend is toward drier conditions but only in MAM does this reach statistical significance. The SST-forced models have significant drying trends in both DJF and MAM. These drying trends in observations and models are consistent with a statistically significant trend in the PDO index.
- For the drought region as a whole, only in MAM is there a suggestion of a human-induced drying trend. This is because the drought region in DJF and MAM spans the northern reach of a human-induced drying trend and the southern reach of a human-induced wetting trend while the human-induced trends in JJA and SON are weak. Consequently, the human-driven climate change component of long-term drying in the drought region appears weaker than that due to natural decadal variability. In contrast, the trend toward warming is clear, in all seasons and supported by all model experiments. This is making droughts hotter although the impacts on, say, soil moisture and runoff were not investigated here.

Our study ends in May 2021 but the drought continued up until the time of writing (July 2022). Although parts of the Southwest had wet conditions in early winter 2021, a second-year La Niña in winter to spring 2022 appears to have once more driven dry conditions in the Southwest extending this drought into its second year. Looking forward it is hard to know when this drought will end. The PDO was mostly in its cool tropical Pacific phase since 1998 and, while briefly in the warm tropics phase around the 2015/16 El Niño, has recently shifted back toward its cold phase, no doubt partly because of the ongoing persistent La Niña. Human-induced drying in the southern portions of the region will strengthen and warming will continue. Also, we should note that it has been argued that a long-term observed trend toward lack of warming or even cooling of the equatorial Pacific cold tongue is, in fact, a coupled atmosphere–ocean dynamical response to rising greenhouse gases (GHGs) (Seager et al. 2019b, 2022). CMIP6 (and earlier generation) models do not capture this trend and instead tend to warm the cold tongue over the historical period and preferentially warm it over future decades (Watanabe et al. 2021). If the models are wrong and the cold tongue, in response to rising GHGs, remains a region of little warming, this would likely induce reduced precipitation in the southwest by analogy to La Niña and the cold tropics phase of the PDO. Hence it is possible that human-induced climate change could produce a tendency to drier conditions (less precipitation) in the Southwest. The best bet for a return to wetter conditions is a warming of the tropical Pacific due to either a PDO shift or a tropical Pacific Ocean response to rising GHGs like that seen in CMIP6 models. However, the persistence of the cool phase of the PDO and the persistence of cool waters in the cold tongue mean that it would be wise to not trust to the luck of natural variability or place faith in CMIP6 model projections but, instead, to recognize that there is a reasonable chance drought conditions will persist into the near future.

Acknowledgments. This work was supported at Lamont by NOAA Award NA20OAR4310379 and NSF Award AGS-2101214. CMIP6 data were retrieved from the Earth System Grid Federation (https://esgf-node.llnl.gov/projects/cmip6/) and the LENS data are from the Mutimodel Large Ensembles Archive (https://www.cesm.ucar.edu/projects/community-projects/MMLEA/) IRS was supported by NOAA Award NA20OAR4310413 and the National Center for Atmospheric Research, which is a major facility sponsored by the National Science Foundation under Cooperative Agreement 1852977.

Data availability statement. Data for observations, reanalyses, SST-forced models, and CMIP6 models are available from the URLs given in section 2 of the paper.

REFERENCES

Adams, D. K., and A. C. Comrie, 1997: The North American monsoon. *Bull. Amer. Meteor. Soc.*, **78**, 2197–2214, https://doi.org/10.1175/1520-0477(1997)078<2197:TNAM>2.0.CO;2.

Ault, T. R., and S. St. George, 2010: The magnitude of decadal and multidecadal variability in North American precipitation. *J. Climate*, **23**, 842–850, https://doi.org/10.1175/2009JCLI3013.1.

Berg, A., B. R. Lintner, K. L. Findell, S. Malyshev, P. C. Loikith, and P. Gentine, 2014: Impact of soil moisture–atmosphere interactions on surface temperature distribution. *J. Climate*, **27**, 7976–7993, https://doi.org/10.1175/JCLI-D-13-00591.1.

Bogenschutz, P., A. Gettelman, C. Hannay, V. E. Larsen, R. Neale, C. Craig, and C. Chen, 2018: The path to CAM6: Coupled simulations with CAM5.4 and CAM5.5. *Geosci. Model Dev.*, **11**, 235–255, https://doi.org/10.5194/gmd-11-235-2018.

CAM Team, 2021: CAM6 (Community Atmosphere Model version 6), model item. OpenGMS, accessed April 2022, https://geomodeling.njnu.edu.cn/modelItem/f36d9d3a-e937-46ac-ba7c-286886ccfad7.

Chen, M., and Coauthors, 2008: CPC unified gauge-based analysis of global daily precipitation. *Western Pacific Geophysics Meeting*, Cairns, Australia, Amer. Geophys. Union, Abstract A24A-05.

Chen, X., and J. M. Wallace, 2015: ENSO-like variability: 1900–2013. *J. Climate*, **28**, 9623–9641, https://doi.org/10.1175/JCLI-D-15-0322.1.

Cheng, L., M. Hoerling, Z. Liu, and J. Eischeid, 2019: Physical understanding of human-induced changes in U.S. hot droughts using equilibrium climate simulations. *J. Climate*, **32**, 4431–4443, https://doi.org/10.1175/JCLI-D-18-0611.1.

Cook, E. R., R. Seager, M. A. Cane, and D. W. Stahle, 2007: North American droughts: Reconstructions, causes, and consequences. *Earth-Sci. Rev.*, **81**, 93–134, https://doi.org/10.1016/j.earscirev.2006.12.002.

Delworth, T. L., F. Zeng, A. Rosati, G. A. Vecchi, and A. T. Wittenberg, 2015: A link between the hiatus in global warming and North American drought. *J. Climate*, **28**, 3834–3845, https://doi.org/10.1175/JCLI-D-14-00616.1.

Douglas, M. W., R. A. Maddox, K. Howard, and S. Reyes, 1993: The Mexican monsoon. *J. Climate*, **6**, 1665–1677, https://doi.org/10.1175/1520-0442(1993)006<1665:TMM>2.0.CO;2.

Eyring, V., S. Bony, G. A. Meehl, C. A. Senior, B. Stevens, R. J. Stouffer, and K. E. Taylor, 2016: Overview of the Coupled Model Intercomparison Project phase 6 (CMIP6) experimental design and organization. *Geosci. Model Dev.*, **9**, 1937–1958, https://doi.org/10.5194/gmd-9-1937-2016.

Feng, S., R. J. Oglesby, C. M. Rowe, D. B. Loope, and Q. Hul, 2008: Atlantic and Pacific SST influences on medieval drought in North America simulated by the Community Atmospheric Model. *J. Geophys. Res.*, **113**, D11101, https://doi.org/10.1029/2007JD009347.

Gao, Y., L. R. Leung, J. Lu, Y. Liu, M. Huang, and Y. Qian, 2014: Robust spring drying in the southwestern US and seasonal migration of wet/dry patterns in a warmer climate. *Geophys. Res. Lett.*, **41**, 1745–1751, https://doi.org/10.1002/2014GL059562.

Garreaud, R. D., and D. S. Battisti, 1999: Interannual (ENSO) and interdecadal (ENSO-like) variability in the Southern Hemisphere tropospheric circulation. *J. Climate*, **12**, 2113–2123, https://doi.org/10.1175/1520-0442(1999)012<2113:IEAIEL>2.0.CO;2.

Gill, A. E., 1980: Some simple solutions for heat-induced tropical circulation. *Quart. J. Roy. Meteor. Soc.*, **106**, 447–462, https://doi.org/10.1002/qj.49710644905.

Herweijer, C., and R. Seager, 2008: The global footprint of persistent extratropical drought in the instrumental era. *Int. J. Climatol.*, **28**, 1761–1774, https://doi.org/10.1002/joc.1590.

——, ——, and E. R. Cook, 2006: North American droughts of the mid to late nineteenth century: A history, simulation and implications for medieval drought. *Holocene*, **16**, 159–171, https://doi.org/10.1191/0959683606hl917rp.

Hoell, A., and Coauthors, 2022: Record low North American monsoon rainfall in 2020 reignites drought over the American Southwest. *Bull. Amer. Meteor. Soc.*, **103**, S26–S32, https://doi.org/10.1175/BAMS-D-21-0129.1.

Hoerling, M. P., J. Eischeid, and J. Perlwitz, 2010: Regional precipitation trends: Distinguishing natural variability from anthropogenic forcing. *J. Climate*, **23**, 2131–2145, https://doi.org/10.1175/2009JCLI3420.1.

——, and Coauthors, 2013: Anatomy of an extreme event. *J. Climate*, **26**, 2811–2832, https://doi.org/10.1175/JCLI-D-12-00270.1.

——, J. Barsugli, B. Livneh, J. Eischeid, X. Quan, and A. Badger, 2019: Causes for the century-long decline in Colorado River flow. *J. Climate*, **32**, 8181–8203, https://doi.org/10.1175/JCLI-D-19-0207.1.

Huang, B., and Coauthors, 2017: Extended Reconstructed Sea Surface Temperature, version 5 (ERSSTv5): Upgrades, validations, and intercomparisons. *J. Climate*, **30**, 8179–8205, https://doi.org/10.1175/JCLI-D-16-0836.1.

Huang, H.-P., R. Seager, and Y. Kushnir, 2005: The 1976/77 transition in precipitation over the Americas and the influence of tropical SST. *Climate Dyn.*, **24**, 721–740, https://doi.org/10.1007/s00382-005-0015-6.

Hurrell, J. W., J. J. Hack, D. Shea, J. M. Caron, and J. Rosinski, 2008: A new sea surface temperature and sea ice boundary data set for the Community Atmosphere Model. *J. Climate*, **21**, 5145–5153, https://doi.org/10.1175/2008JCLI2292.1.

Kalnay, E., and Coauthors, 1996: The NCEP/NCAR 40-Year Reanalysis Project. *Bull. Amer. Meteor. Soc.*, **77**, 437–472, https://doi.org/10.1175/1520-0477(1996)077<0437:TNYRP>2.0.CO;2.

Kanamitsu, M., W. Ebisuzaki, J. Woollen, S.-K. Yang, J. J. Hnilo, M. Fiorino, and G. L. Potter, 2002: NCEP–DOE AMIP-II reanalysis (R-2). *Bull. Amer. Meteor. Soc.*, **83**, 1631–1644, https://doi.org/10.1175/BAMS-83-11-1631.

Kennedy, J. J., N. A. Rayner, R. O. Smith, D. E. Parker, and M. Saunby, 2011a: Reassessing biases and other uncertainties in sea surface temperature observations since 1850: 1. Measurement and sampling uncertainties. *J. Geophys. Res.*, **116**, D14103, https://doi.org/10.1029/2010JD015218.

——, ——, ——, ——, and ——, 2011b: Reassessing biases and other uncertainties in sea surface temperature observations since 1850: 2. Biases and homogenization. *J. Geophys. Res.*, **116**, D14104, https://doi.org/10.1029/2010JD015220.

Kiehl, J. T., J. J. Hack, G. B. Bonan, B. A. Bovile, D. L. Williamson, and P. J. Rasch, 1998: The National Center for Atmospheric Research Community Climate Model: CCM3. *J. Climate*, **11**, 1131–1149, https://doi.org/10.1175/1520-0442(1998)011<1131:TNCFAR>2.0.CO;2.

Kistler, R., and Coauthors, 2001: The NCEP–NCAR 50-Year Reanalysis: Monthly means CD-ROM and documentation. *Bull. Amer. Meteor. Soc.*, **82**, 247–268, https://doi.org/10.1175/1520-0477(2001)082<0247:TNNYRM>2.3.CO;2.

Koster, R. D., S. D. Schubert, and M. J. Suarez, 2009: Analyzing the concurrence of meteorological droughts and warm periods, with implications for the determination of evaporative regime. *J. Climate*, **22**, 3331–3341, https://doi.org/10.1175/2008JCLI2718.1.

Kumar, A., and M. P. Hoerling, 1998: Annual cycle of Pacific–North American seasonal predictability associated with different phases of ENSO. *J. Climate*, **11**, 3295–3308, https://doi.org/10.1175/1520-0442(1998)011<3295:ACOPNA>2.0.CO;2.

Lau, N.-C., A. Leetmaa, M. J. Nath, and H.-L. Wang, 2005: Influences of ENSO-induced Indo–western Pacific SST anomalies on extratropical atmospheric variability during the boreal summer. *J. Climate*, **18**, 2922–2942, https://doi.org/10.1175/JCLI3445.1.

Lehner, F., C. Deser, I. R. Simpson, and L. Terray, 2018: Attributing the U.S. Southwest's recent shift into drier conditions. *Geophys. Res. Lett.*, **45**, 6251–6261, https://doi.org/10.1029/2018GL078312.

Maloney, E. D., and Coauthors, 2014: North American climate in CMIP5 experiments: Part III: Assessment of twenty-first-century projections. *J. Climate*, **27**, 2230–2270, https://doi.org/10.1175/JCLI-D-13-00273.1.

Mankin, J. S., I. Simpson, A. Hoell, R. Fu, J. Lisonbee, A. Sheffield, and D. Barrie, 2021: NOAA Drought Task Force Report on the 2020–2021 southwestern U.S. drought. National Oceanic and Atmospheric Administration Drought Task Force, Modeling Analysis Predictability and Prediction, National Integrated Drought Information System, Tech. Rep., 20 pp., https://www.drought.gov/sites/default/files/2021-09/NOAA-Drought-Task-Force-IV-Southwest-Drought-Report-9-23-21.pdf.

Mantua, N. J., and S. R. Hare, 2002: The Pacific decadal oscillation. *J. Oceanogr.*, **58**, 35–44, https://doi.org/10.1023/A:1015820616384.

——, ——, Y. Zhang, J. M. Wallace, and R. C. Francis, 1997: A Pacific interdecadal climate oscillation with impacts on salmon production. *Bull. Amer. Meteor. Soc.*, **78**, 1069–1080, https://doi.org/10.1175/1520-0477(1997)078<1069:APICOW>2.0.CO;2.

McAfee, S. A., 2014: Consistency and the lack thereof in Pacific decadal oscillation impacts on North American winter climate. *J. Climate*, **27**, 7410–7431, https://doi.org/10.1175/JCLI-D-14-00143.1.

McKinnon, K. A., A. Poppick, and I. R. Simpson, 2021: Hot extremes have become drier in the United States Southwest. *Nat. Climate Change*, **11**, 598–604, https://doi.org/10.1038/s41558-021-01076-9.

Newman, M., and Coauthors, 2016: The Pacific decadal oscillation, revisited. *J. Climate*, **29**, 4399–4427, https://doi.org/10.1175/JCLI-D-15-0508.1.

Okumura, Y., P. DiNezio, and C. Deser, 2017: Evolving impacts of multiyear La Niña events on atmospheric circulation and U.S. drought. *Geophys. Res. Lett.*, **44**, 11 614–11 623, https://doi.org/10.1002/2017GL075034.

Ropelewski, C. F., J. E. Janowiak, and M. S. Halpert, 1985: The analysis and display of real time surface climate data. *Mon. Wea. Rev.*, **113**, 1101–1106, https://doi.org/10.1175/1520-0493(1985)113<1101:TAADOR>2.0.CO;2.

Schubert, S. D., M. J. Suarez, P. J. Pegion, R. D. Koster, and J. T. Bacmeister, 2004a: Causes of long-term drought in the United States Great Plains. *J. Climate*, **17**, 485–503, https://doi.org/10.1175/1520-0442(2004)017<0485:COLDIT>2.0.CO;2.

——, ——, ——, ——, and ——, 2004b: On the cause of the 1930s Dust Bowl. *Science*, **303**, 1855–1859, https://doi.org/10.1126/science.1095048.

——, and Coauthors, 2009: A U.S. CLIVAR project to assess and compare the responses of global climate models to drought-related SST forcing patterns: Overview and results. *J. Climate*, **22**, 5251–5272, https://doi.org/10.1175/2009JCLI3060.1.

Seager, R., 2015: Decadal hydroclimate variability across the Americas. *Climate Change: Multidecadal and Beyond*, C.-P. Chang et al., Eds., World Scientific, 235–254.

——, and M. P. Hoerling, 2014: Atmosphere and ocean origins of North American drought. *J. Climate*, **27**, 4581–4606, https://doi.org/10.1175/JCLI-D-13-00329.1.

——, Y. Kushnir, C. Herweijer, N. Naik, and J. Velez, 2005: Modeling of tropical forcing of persistent droughts and pluvials over western North America: 1856–2000. *J. Climate*, **18**, 4065–4088, https://doi.org/10.1175/JCLI3522.1.

——, R. Burgman, Y. Kushnir, A. Clement, E. Cook, N. Naik, and J. Velez, 2008: Tropical Pacific forcing of North American medieval megadroughts: Testing the concept with an atmosphere model forced by coral-reconstructed SSTs. *J. Climate*, **21**, 6175–6190, https://doi.org/10.1175/2008JCLI2170.1.

——, L. Goddard, J. Nakamura, N. Naik, and D. E. Lee, 2014a: Dynamical causes of the 2010/11 Texas–northern Mexico drought. *J. Hydrometeor.*, **15**, 39–68, https://doi.org/10.1175/JHM-D-13-024.1.

——, and Coauthors, 2014b: Dynamical and thermodynamical causes of large-scale changes in the hydrological cycle over North America in response to global warming. *J. Climate*, **27**, 7921–7948, https://doi.org/10.1175/JCLI-D-14-00153.1.

——, N. Henderson, M. Cane, H. Liu, and J. Nakamura, 2017: Is there a role for human-induced climate change in the precipitation decline that drove the California drought? *J. Climate*, **30**, 10 237–10 258, https://doi.org/10.1175/JCLI-D-17-0192.1.

——, M. Cane, N. Henderson, D.-E. Lee, R. Abernathey, and H. Zhang, 2019a: Strengthening tropical Pacific zonal sea surface temperature gradient consistent with rising greenhouse gases. *Nat. Climate Change*, **9**, 517–522, https://doi.org/10.1038/s41558-019-0505-x.

——, T. J. Osborn, Y. Kushnir, I. R. Simpson, J. Nakamura, and H. Liu, 2019b: Climate variability and change of Mediterranean-type climates. *J. Climate*, **32**, 2887–2915, https://doi.org/10.1175/JCLI-D-18-0472.1.

——, N. Henderson, and M. A. Cane, 2022: Persistent discrepancies between observed and modeled trends in the tropical Pacific Ocean. *J. Climate*, **35**, 4571–4584, https://doi.org/10.1175/JCLI-D-21-0648.1.

Shin, S.-I., and P. D. Sardeshmukh, 2011: Critical influence of the pattern of tropical ocean warming on remote climate trends. *Climate Dyn.*, **36**, 1577–1591, https://doi.org/10.1007/s00382-009-0732-3.

——, ——, and R. S. Webb, 2010: Optimal tropical sea surface temperature forcing of North American drought. *J. Climate*, **23**, 3907–3917, https://doi.org/10.1175/2010JCLI3360.1.

Swetnam, T. W., and J. L. Betancourt, 1998: Mesoscale disturbance and ecological response to decadal climate variability in the American Southwest. *J. Climate*, **11**, 3128–3147, https://doi.org/10.1175/1520-0442(1998)011<3128:MDAERT>2.0.CO;2.

Ting, M., R. Seager, C. Li, H. Liu, and N. Henderson, 2018: Mechanisms of future spring drying in the southwestern United States in CMIP5 models. *J. Climate*, **31**, 4265–4279, https://doi.org/10.1175/JCLI-D-17-0574.1.

——, ——, ——, ——, and ——, 2021: Future summer drying in the U.S. Corn Belt and the role of mid-latitude storm tracks. *J. Climate*, **34**, 9043–9056, https://doi.org/10.1175/JCLI-D-20-1004.1.

Watanabe, M., J.-L. Dufresne, Y. Kosaka, T. Mauritsen, and H. Tatebe, 2021: Enhanced warming constrained by past trends in equatorial Pacific sea surface temperature gradient. *Nat. Climate Change*, **11**, 33–37, https://doi.org/10.1038/s41558-020-00933-3.

Wilks, D. S., 1995: *Statistical Methods in the Atmospheric Sciences: An Introduction*. Academic Press, 467 pp.

Williams, A. P., and Coauthors, 2020: Large contribution from anthropogenic warming to an emerging North American megadrought. *Science*, **368**, 314–318, https://doi.org/10.1126/science.aaz9600.

——, B. I. Cook, and J. E. Smerdon, 2022: Rapid intensification of the emerging southwestern North American megadrought in 2020–21. *Nat. Climate Change*, **12**, 232–234, https://doi.org/10.1038/s41558-022-01290-z.

Xiao, M., B. Udall, and D. P. Lettenmaier, 2018: On the causes of declining Colorado River streamflows. *Water Resour. Res.*, **54**, 6739–6756, https://doi.org/10.1029/2018WR023153.

Xie, P., and P. A. Arkin, 1996: Analyses of global monthly precipitation using gauge observations, satellite estimates, and numerical model predictions. *J. Climate*, **9**, 840–858, https://doi.org/10.1175/1520-0442(1996)009<0840:AOGMPU>2.0.CO;2.

——, and ——, 1997: Global precipitation: A 17-year monthly analysis based on gauge observations, satellite estimates, and numerical model outputs. *Bull. Amer. Meteor. Soc.*, **78**, 2539–2558, https://doi.org/10.1175/1520-0477(1997)078<2539:GPAYMA>2.0.CO;2.

Yin, D., M. L. Roderick, G. Leech, F. Sun, and Y. Huang, 2014: The contribution of reduction in evaporative cooling to higher surface air temperatures during drought. *Geophys. Res. Lett.*, **41**, 7891–7897, https://doi.org/10.1002/2014GL062039.

Zhang, Y., J. M. Wallace, and D. S. Battisti, 1997: ENSO-like decade-to-century scale variability: 1900–93. *J. Climate*, **10**, 1004–1020, https://doi.org/10.1175/1520-0442(1997)010<1004:ELIV>2.0.CO;2.